AGU PUBLICATIONS

JGR

Journal of Geophysical Research: Atmospheres

RESEARCH ARTICLE
10.1002/2015JD024212

Special Section:
Energetic Electron Loss and its Impacts on the Atmosphere

A model providing long-term data sets of energetic electron precipitation during geomagnetic storms

M. van de Kamp[1], A. Seppälä[1], M. A. Clilverd[2], C. J. Rodger[3], P. T. Verronen[1], and I. C. Whittaker[4]

[1]Finnish Meteorological Institute, Helsinki, Finland, [2]British Antarctic Survey/NERC, Cambridge, UK, [3]Department of Physics, University of Otago, Dunedin, New Zealand, [4]Department of Physics and Astronomy, University of Leicester, Leicester, UK

Key Points:
- A model for radiation belt energetic electron precipitation (30-1000 keV) has been developed
- It can be used to calculate the energy-flux spectrum of precipitating electron from 1932 to present
- The results can be used to produce the first >80 year long atmospheric ionization rate data set

Correspondence to:
A. Seppälä,
annika.seppala@fmi.fi

Citation:
van de Kamp, M., A. Seppälä, M. A. Clilverd, C. J. Rodger, P. T. Verronen, and I. C. Whittaker (2016), A model providing long-term data sets of energetic electron precipitation during geomagnetic storms, *J. Geophys. Res. Atmos.*, *121*, 12,520–12,540, doi:10.1002/2015JD024212.

Received 14 SEP 2015
Accepted 2 OCT 2016
Accepted article online 6 OCT 2016
Published online 26 OCT 2016

Abstract The influence of solar variability on the polar atmosphere and climate due to energetic electron precipitation (EEP) has remained an open question largely due to lack of a long-term EEP forcing data set that could be used in chemistry-climate models. Motivated by this, we have developed a model for 30–1000 keV radiation belt driven EEP. The model is based on precipitation data from low Earth orbiting POES satellites in the period 2002–2012 and empirically described plasmasphere structure, which are both scaled to a geomagnetic index. This geomagnetic index is the only input of the model and can be either *Dst* or *Ap*. Because of this, the model can be used to calculate the energy-flux spectrum of precipitating electrons from 1957 (*Dst*) or 1932 (*Ap*) onward, with a time resolution of 1 day. Results from the model compare well with EEP observations over the period of 2002–2012. Using the model avoids the challenges found in measured data sets concerning proton contamination. As demonstrated, the model results can be used to produce the first ever >80 year long atmospheric ionization rate data set for radiation belt EEP. The impact of precipitation in this energy range is mainly seen at altitudes 70–110 km. The ionization rate data set, which is available for the scientific community, will enable simulations of EEP impacts on the atmosphere and climate with realistic EEP variability. Due to limitations in this first version of the model, the results most likely represent an underestimation of the total EEP effect.

1. Introduction

After the discovery of the effects that solar proton events (SPEs) have on mesospheric ozone balance in sounding rocket experiments [*Weeks et al.*, 1972] our understanding of the influence that energetic particle precipitation (EPP) has on the atmosphere has increased significantly. We now understand that EPP provides an important source of odd hydrogen (HO_x) and odd nitrogen (NO_x) in the polar middle atmosphere, between the altitudes of about 30 and 90 km. These in turn influence the polar ozone balance via several chemical reactions and catalytic reaction chains.

Much work has been done to include the effect of proton deposition into atmospheric models [*Jackman et al.*, 2008, 2009; *Neal et al.*, 2013; *Nesse Tyssøy and Stadsnes*, 2015]. Meanwhile, it has also become clear that SPEs are not the sole source of EPP into the atmosphere. Electron precipitation contributes to ionizaton as well [e.g., *Spjeldvik and Thorne*, 1976] and to the formation of NO_x [*Callis et al.*, 1996]. It is now apparent that when long-term (months–years) impacts are considered, the precipitation of energetic electrons may be at least as important as protons [*Funke et al.*, 2014a; *Andersson et al.*, 2014]. Several studies have addressed the so-called EPP indirect effect [*Randall et al.*, 2007], which takes into account the consequences beyond the initial EPP impact region via coupling to atmospheric dynamics and transport of chemically active species, such as NO_x. In a recent study, *Randall et al.* [2015] highlighted the importance of the roles of both atmospheric dynamical events and the missing EPP contribution from energetic electron precipitation (EEP) in order to correctly simulate the polar winter stratosphere-mesosphere region.

Additional interest for inclusion of EPP (SPE + EEP) in atmospheric models arises from results suggesting links coupling the initial polar middle atmosphere chemical changes to dynamical variables in the stratosphere, propagating down to the troposphere and ground level. The impacts of these are similar in magnitude to those arising from variations in solar spectral irradiance [e.g., *Rozanov et al.*, 2012; *Seppälä and Clilverd*, 2014; *Seppälä et al.*, 2014]. Thus, EPP potentially provides a pathway from the Sun via magnetospheric processes into polar climate variability [*Seppälä et al.*, 2009, 2013]. These linkages are not yet fully understood mainly

due to the limited capability of chemistry-climate models to include a full description of EPP and its long-term variability [*Seppälä et al.*, 2014].

Currently, most of the "high-top" models (chemistry-climate models with upper boundary in the mesosphere or above), such as ECHAM5/MESSy [*Baumgaertner et al.*, 2011] and WACCM [*Jackman et al.*, 2009], include SPEs as one of the EPP sources producing HO_x and NO_x. In addition, some, such as WACCM, include lower energy (auroral) electron and proton precipitation, parameterized by geomagnetic activity proxies, as the thermospheric NO_x source. However, inclusion of medium- and high-energy electrons has remained a challenge. In the absence of long-term observations of energetic electron fluxes into the atmosphere, proxies that describe the overall impact of energetic particle effects on the atmosphere have been developed. These are mainly limited to estimating the variability of NO_x levels in terms of changes in geomagnetic activity as the two are known to be closely linked [*Randall et al.*, 2007]. For model simulations, proxies for EEP-induced NO_x production have been developed, most recently by *Baumgaertner et al.* [2009] and *Funke et al.* [2014b]. While these proxies can be used in long-term simulations, they are, however, limited in the sense that they only provide an estimate of the EPP-NO_x (or NO_y) at the model upper boundary and cannot resolve the in situ vertical production by medium- to high-energy electrons. Information concerning this vertical production is important as it affects how rapidly the EPP-NO_x can reach stratospheric altitudes. For HO_x, which is also very important for the atmospheric ozone balance especially at mesospheric altitudes [*Verronen et al.*, 2006, 2011; *Andersson et al.*, 2014], this type of proxy driven upper boundary source approach is invalid due to its very short chemical lifetime. The best way of establishing the long-term variability of middle atmosphere EPP-HO_x, and its impact on ozone levels and beyond, is to establish an altitude-dependent EEP forcing data set and thus including the in situ HO_x production.

Several models have been developed which describe EEP patterns as functions of geomagnetic activity, based on statistical analysis of NOAA satellite observations [e.g., *Codrescu et al.*, 1997; *Wüest et al.*, 2005; *Wissing and Kallenrode*, 2009]. Rather than using one of these models, we chose to develop a new model specifically for our purpose.

The precipitation of medium- and high-energy electrons into the Earth's atmosphere is concurrent with the level of geomagnetic activity and geomagnetic storms and substorms, which are caused by the same magnetospheric processes. Within the geomagnetic field energetic electrons are trapped, transported, and energized in the Van Allen Belts by processes such as radial diffusion and very low frequency waves (VLF) [*Thorne*, 2010]. During periods of high geomagnetic activity the fluxes of energetic electrons in the outer radiation belt can change by orders of magnitude in hours or possibly minutes. Some of the flux variability is caused by the loss of electrons into the atmosphere; the magnetic latitude of the outer radiation belt is such that most of these electrons enter the atmosphere at high latitudes in both the northern and southern magnetic hemispheres.

Processes that drive electron precipitation such as VLF whistler mode chorus waves, plasmaspheric hiss waves, and electromagnetic ion-cyclotron (EMIC) waves [*Summers et al.*, 2007], are strongly influenced by the background density of nonenergetic electrons within the inner magnetosphere—where the dense part is known as the plasmasphere [*Carpenter*, 1963]. Plasmaspheric hiss processes that dominate within the plasmasphere produce only low levels of precipitation flux. EMIC-driven precipitation processes are focused close to the outer edge of the plasmasphere [*Carson et al.*, 2013]. They produce highly energetic electron precipitation, but are restricted to a region that is small spatially [*Clilverd et al.*, 2015]. Chorus waves are believed to dominate electron precipitation processes outside of the plasmasphere and produce high fluxes of electron precipitation with large spatial extent [*Whittaker et al.*, 2014a]. The level of geomagnetic activity is not only correlated with the magnitude of electron precipitation into the atmosphere but also with the position of the plasmapause, i.e., the boundary between the dense plasmasphere and the less dense regions farther from the Earth [e.g., *O'Brien and Moldwin*, 2003].

The current study is focused on EEP in the energy range 30–1000 keV. The lower limit of this chosen range is equal to that of the measurement instruments used (see below); the upper limit is applied because above 1 MeV, the fluxes due to chorus waves become very small (see next section) and different processes, such as EMIC waves, significantly start to contribute, which show a different behavior dependent on location and disturbance level, as shown by, e.g., *Summers et al.* [2007].

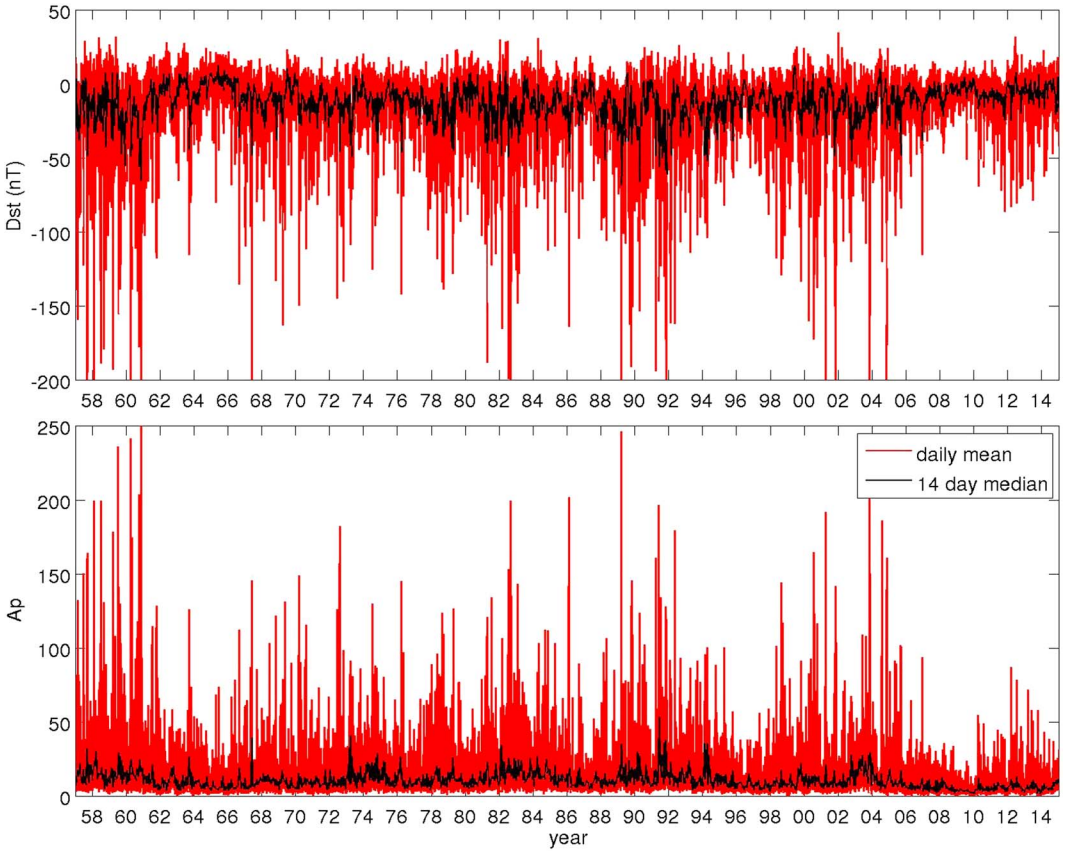

Figure 1. *Dst* and *Ap* time series for the period for which the *Dst* index is available. The red lines present the daily mean, while the black lines correspond to 14 day medians, included for clarity.

In order to obtain EEP data as input to an atmospheric model dependent on location, time, and geomagnetic activity, direct satellite measurements are useful, such as the NOAA TIROS data of 1984 used by *Callis* [1997]. However, to undertake long-term simulations of the influence of geomagnetic activity on the atmosphere it is necessary to describe the variability of the EEP forcing over decadal timescales. The most useful long-term measurement of EEP is currently provided by the NOAA POES constellation, with several satellites at different Sun-synchronous polar orbits. The satellites carry electron telescopes capable of measuring the medium energy electron fluxes (30 keV–2.5 MeV) that enter into the atmosphere, in the SEM-2 instrument package [*Rodger et al.*, 2010a, 2010b; *Yando et al.*, 2011]. However, the SEM-2 instrument on board POES, which is a significant upgrade from the SEM-1 package, which operated on board earlier NOAA satellites, has been providing measurements only since 1998. Furthermore, during this period initially, only a few satellite observational platforms were in operation, so that a useful globally covering EEP data set is available only from about 2002. Therefore, to provide decadal EEP descriptions an alternative technique must be developed.

Whittaker et al. [2014a] used POES electron precipitation observations to show that knowledge of geomagnetic conditions and of the location of the plasmapause can be used to derive simple expressions for the electron precipitation (>30 keV) associated with whistler mode chorus and plasmaspheric hiss. In this study we build on this understanding of the electron precipitation processes, including the importance of the location of the plasmapause, to identify the main electron precipitation characteristics that are required for atmospheric models, i.e., geographical location, temporal variation, and electron energy spectrum. Given the correlation between geomagnetic indices and the strength of electron precipitation [e.g., *Whittaker et al.*, 2014a], the significant influence of the location of the plasmapause on the processes that precipitate electrons into the atmosphere [*Hardman et al.*, 2015], and the ability to describe plasmapause dynamics through geomagnetic indexes, it should be possible to describe EEP using an appropriate long-term geomagnetic index.

Fortunately, high-quality geomagnetic indexes were developed as part of the International Geophysical year in 1957, and several are now more than 50 years in length. *Ap*, *Kp*, *Dst* (disturbance storm time index), and *AE* (auroral electrojet index) are all long-term geomagnetic activity data sets [*Mayaud*, 1980] that have been used to represent the dynamical behavior of the plasmapause [e.g., *Carpenter and Anderson*, 1992; *O'Brien and Moldwin*, 2003]. The globally calculated hourly *Dst* index also provides a quantitative measure of the severity of magnetic storms, particularly those driven by coronal mass ejections [*Borovsky and Denton*, 2006]. Dependent on the type of magnetic storms, different geomagnetic indices may be the best indicators of the disturbance and hence of the particle precipitation caused by it. An analysis of these goes beyond the scope of this paper, as the purpose of this study is to provide a long-term data set. This makes a practical argument significant: both the *Dst* index and the daily *Ap* (effective daily values calculated from the 3-hourly *Kp* index) provide a >50 year uninterrupted data series, which make them useful as inputs in long-term chemistry-climate models. Figure 1 shows the variations of the *Dst* and *Ap* indices since 1957, with nondisturbed geomagnetic conditions represented by values close to zero, and large geomagnetic storms indicated by about $Dst < -50$ nT and $Ap > 50$ (for the daily mean values). An 11 year cycle can be seen in the occurrence of large geomagnetic storms.

Summarizing, following the discovery of *Andersson et al.* [2014], which identified electron precipitation from the Earth's radiation belts as a significant but previously missing source for important ozone loss at mesospheric altitudes, there is motivation in establishing a long-term EEP data set that could be utilized in chemistry-climate model simulations. This data set would also respond to the issue concerning production of EPP-HO_x and potentially help resolve the early timing of the appearance of middle atmosphere dynamical changes arising from EPP, which could not be explained by EPP-NO_x transport to stratospheric altitudes [*Lu et al.*, 2008; *Seppälä et al.*, 2013].

The following sections of this paper describe the available data set of satellite observations, the EEP model developed based on the underlying plasmaspheric structure and geomagnetic activity, and the resultant long-term ionization rate data set that can be used as an input to coupled chemistry-climate models.

2. POES/SEM Electron Flux Measurement

2.1. Observations

The NOAA Polar Orbiting Environmental Satellites (POES) (http://www.ospo.noaa.gov/Operations/POES/) circle the Earth approximately 14 times a day in Sun-synchronous polar orbits at ~800–850 km altitudes. On board these satellites is the Space Environment Monitor (SEM-2) [*Evans and Greer*, 2004; *Rodger et al.*, 2010a], which contains the Medium-Energy Proton and Electron Detector (MEPED). The three electron detectors included in MEPED count detected electrons in three energy pass bands: >30 keV, >100 keV, and >300 keV. The nominal upper energy limit is 2500 keV for all three electron detectors [*Evans and Greer*, 2004], although higher-energy electrons can also enter the detectors as shown by *Yando et al.* [2011]. For each energy band, two identical detectors are mounted at right angles of each other: one pointing 9° off from vertically upward (away from Earth), the other 9° off from antiparallel to the spacecraft motion. Both telescopes have a field of view that is 30° wide and have a temporal resolution of 2 s. At the latitudes of the outer radiation belt and the auroral zone, the near-vertically pointing detector measures some of the electrons that are likely to enter the atmosphere shortly after, i.e., a portion of the bounce loss cone [*Rodger et al.*, 2010b]. The location of each measurement point was converted to McIlwain *L* shell values (referred henceforth to as *L* shell, or *L*) [*McIlwain*, 1961] using the IGRF model of the magnetic field and the National Science Data Center INVAR program [*Evans and Greer*, 2004; *Lam et al.*, 2010]. The MEPED instruments on board the different satellites have all been built at the same time and cross calibrated on the ground. In addition, the instruments undergo a weekly in-flight calibration procedure, which involves stimulating each detector with pulses of known amplitude, to check its response sensitivity. Further, detailed technical description of the SEM-2 measurement instrument is given by *Evans and Greer* [2004], including calibration and the conversion from detected electron counts to fluxes in units of electrons cm^{-2} sr^{-1} s^{-1}.

The electron counts measured by MEPED represent the average flux over the detector aperture, which is equal to the average flux over the entire bounce loss cone if a uniform population of the bounce loss cone can be assumed. During strong disturbances, angle diffusion is strong, making this assumption justified. However, during weaker disturbances, weak diffusion keeps the electrons mainly near the edge of the bounce loss cone, and away from the detector, which causes an underestimate of these fluxes. *Rodger et al.* [2013]

analyzed this effect for substorms, and *Simon Wedlund et al.* [2014] for radiation belt precipitation. They reached different results for the threshold value and the correction factors for this effect, due to the different types of scattering/diffusion taking place. *Nesse Tyssøy et al.* [2016] showed in Figure 6 of their paper that the diffusion strength is similar between the three energy ranges of the MEPED detectors. A full test of the correction for all POES fluxes at all L shells and at all MLT still needs to be done. At this point, it can only be said as a rough estimate that observed fluxes below about 10^4 to 10^5 electrons cm^{-2} sr^{-1} s^{-1} may be underestimating the loss cone fluxes by up to a factor of about 10.

The MEPED electron detectors are subject to varying levels of false counts from proton contamination [*Rodger et al.*, 2010a; *Yando et al.*, 2011], either from low-energy ring current protons, or high-energy protons during solar proton events. This situation can be detected using the proton flux telescopes on MEPED. Outside of the high fluxes involved in SPEs, the proton contamination can be removed using the equations given by *Lam et al.* [2010]. The accuracy of these corrections to the flux have been checked by a multispacecraft comparison between POES and DEMETER [*Whittaker et al.*, 2014b], using the Monte Carlo contamination simulations of *Yando et al.* [2011]. In the case of very high proton flux levels, such as during SPE, the electron count is dominated by protons and correction would be unreliable. Because of this, all samples concurrent with observations on the MEPED >36 MeV proton detector >3 counts/s have been removed from the POES electron data set. We found that this adequately removes the data dominated by SPE. As a result of this, data measured in and around the South Atlantic Anomaly (SAA) were entirely removed due to the large amount of proton contamination occurring there [*Rodger et al.*, 2013].

This study makes use of the data measured by SEM-2/MEPED on board POES from 2002 to 2012. During this time, the number of measuring satellites increased from two at the start and three from July 2002 to six at the end. All electron precipitation flux measurements were binned as a function of their IGRF L value, covering $L = 2-10$ with resolution 0.5, and as a function of UT time, with a 3 h resolution, and for all MLTs together. The L shell range used covers both the outer radiation belt and the dynamical range of the plasmapause ($2.5 < L < 6$). For each bin, the median electron flux is calculated. Next, in order to obtain daily fluxes, the eight 3 h flux values were linearly averaged over each day, for each energy channel, and each L value.

Each satellite traverses the L shells of the outer radiation belt 4 times in each orbit, and therefore, each 1 day sample involves the averaging of roughly 100 to 300 individual passes through the radiation belts. The Sun-synchronous satellites pass through the radiation belts at fixed geographic local times. From July 2002 onward, there are passes at least at $3 \times 4 = 12$ local times, which are evenly distributed around the clock (only up to June 2002 slightly less so). Furthermore, the globally varying offset between the magnetic and geographic coordinates makes the satellites cover a wide range of magnetic local times (MLT) in 14 passes per day.

In cases of low electron fluxes, the detector is limited by the instrument noise floor. Because of this, all data points where the precipitating electron flux >30 keV was lower than ~250 electrons cm^{-2} sr^{-1} s^{-1}, were removed and replaced by zeros in all three energy ranges.

From the three energy ranges measured by POES SEM-2 it is possible to fit an energy flux spectrum. In a previous measurement campaign, the satellite DEMETER measured the much higher fluxes of precipitating electrons in the drift loss cone at very high spectral resolution [*Whittaker et al.*, 2013]. Differential spectral flux observations from this campaign showed that a power law relationship is appropriate for precipitating electrons in the medium-energy range in the outer radiation belt [*Clilverd et al.*, 2010]. A simple power law model for the spectral density S of the flux is therefore assumed:

$$S(E) = CE^k \qquad \text{electrons}/(\text{cm}^2\ \text{sr}\ \text{s}\ \text{keV}) \tag{1}$$

where E is the energy of the electrons (keV), C is an offset, and k is the spectral gradient. This spectral density can be integrated to obtain the integrated flux as measured between two energy levels:

$$\begin{aligned} F(E) &= \int_E^{E_u} S(E')\mathrm{d}E' && \text{electrons}/(\text{cm}^2\text{sr}\ \text{s}) \\ &= \frac{C}{k+1}(E_u^{k+1} - E^{k+1}) && (k \neq -1) \\ &= C(\ln(E_u) - \ln(E)) && (k = -1). \end{aligned} \tag{2}$$

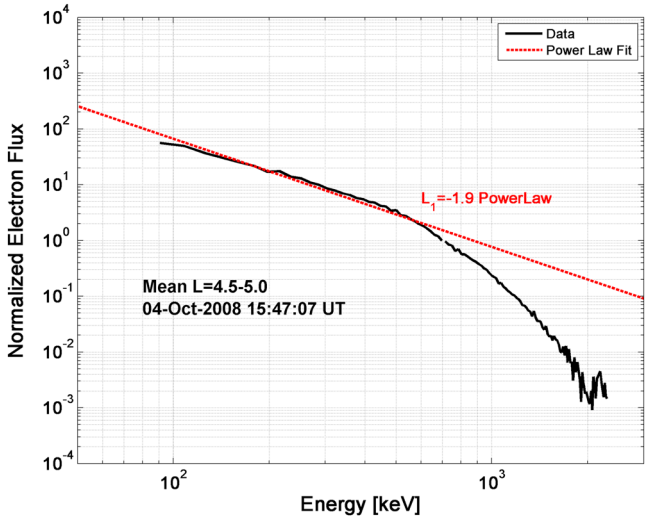

Figure 2. Typical example of the differential flux of precipitating electrons measured by DEMETER in the outer radiation belt. In this case the flux has been normalized by the 700 keV value, and a power law (red line) fitted to the <700 keV fluxes.

However, this is not accurate for relativistic electrons. At these higher energies (above 700–800 keV) the DEMETER spectrum commonly falls off much faster with energy than predicted by a power law; a typical example is shown in Figure 2. The energy threshold where this steep decrease occurs varies, and we use 1000 keV as a representative energy for when the power law typically becomes invalid. Therefore, although the upper energy limit of the electron detector sensitivity is at least 2.5 MeV as mentioned before, it is realistic to approximate the upper limit E_u of the spectrum in equation (2) to be 1 MeV. (Although this may be a rough approximation, it has been tested that the results presented in this paper do not significantly depend on the exact value of E_u, be it 1 or 2.5 MeV, and therefore also not on the shape of the upper limit, be it a sharp cutoff of a steep slope. This is due to the fact that the contribution of the energies above 1 MeV in equation (2) is in any case very small.)

At all data points (i.e., for each time/L value), the function of equation (2) has been fitted to the three measured integrated electron fluxes. Here E is equal to the lower energy threshold of the three detectors (30 keV, 100 keV, and 300 keV), and $E_u = 1000$ keV. The output of this procedure is expressed in the spectral gradient k and the flux >30 keV (F_{30}) resulting from the fit, which is given as a function of C and k by

$$\begin{aligned} F_{30} &= \frac{C}{k+1}\left(1000^{k+1} - 30^{k+1}\right) \quad \text{electrons}/(\text{cm}^2\text{sr s}) \quad (k \neq -1) \\ &= C(\ln(1000) - \ln(30)) \quad \text{electrons}/(\text{cm}^2\text{sr s}) \quad (k = -1). \end{aligned} \tag{3}$$

F_{30} and k are available for every point in time and every value of L.

Typically, the power law gradient k of the energy spectrum varies from −1 to −4 [*Clilverd et al.*, 2010; *Simon Wedlund et al.*, 2014]. At low flux levels some of the three energy ranges could have flux values that are affected by the instrument noise floor, and thus produce an unrealistic power law gradient of ~0; small amounts of noise can produce even more unrealistic positive gradients. However, measurements of precipitating electron fluxes by DEMETER at a much higher spectral resolution [*Clilverd et al.*, 2010] indicated that a reasonable upper limit of the spectral gradient is about −1. Therefore, the maximum value of k in the fitting procedure above has been set to −1. In cases where the three measured fluxes do not fit well to one power law function, the flux >300 keV is assumed to be affected by noise and the fit is performed only on the >30 keV and >100 keV fluxes. This noise influence was detected as the increased probability of the point at 300 keV to be above the fitted curve, dependent on the mean square error of the curve and the flux >300 keV; this happened roughly whenever the flux >300 keV was below 250 electrons cm^{-2} sr^{-1} s^{-1}.

At the end of the process which identifies and compensates for proton contamination, low flux periods, and unrealistic spectral gradients, we are able to produce a 10 year data set with 1 day time resolution, of F_{30} (flux >30 keV electrons cm^{-2} sr^{-1} s^{-1}), and k (power law spectral gradient), calculated for each 0.5 L bin. The data

resulting from this process will be referred to as "modified POES data." There is no magnetic local time (MLT) information available due to the zonal averaging of the satellite observations.

2.2. Validating the Modified POES Fluxes

A recent long-term comparison has been presented between the energetic particle precipitation measurements from POES SEM-2 and those derived from ground-based subionospheric VLF measurements. *Neal et al.* [2015] used VLF amplitude observations made by the AARDDVARK network and updated the approach of *Clilverd et al.* [2010] to extract hourly >30 keV electron precipitation flux values for $L = 3–7$. While the data analysis and modeling approaches presented by *Neal et al.* [2015] are limited to the Northern Hemisphere summer period when the *D* region is sunlit, the AARDDVARK measurements span 2005–2013, and thus provide a long-term set independent of the POES electron precipitation observations. The calculation was done using a combination of models, among which a propagation model of the lower part of the *D* region and a model for the electron density profile dependent on EEP flux, which together give the received VLF amplitude as a function of the EEP spectrum characterized by the parameters F_{30} and k. Inversion of this combined model gave F_{30} as a function of VLF amplitude, if k is given. More details of the procedure are given by *Neal et al.* [2015] and *Rodger et al.* [2012].

Calculation of the AARDDVARK-derived fluxes uses the spectral gradient k provided by the modified POES electron precipitation data set, in order to determine the flux >30 keV which caused the observed VLF amplitude perturbations. When the POES-derived fluxes were set to zero, a power law spectral gradient of −1 was assumed, as discussed above, and used in the AARDDVARK precipitation flux calculations.

Unfortunately, the use of the POES spectra in the AARDDVARK calculations violates the mutual independence of the two data sets. As such, the AARDDVARK fluxes can not be used to completely validate the POES fluxes. However, the greatest uncertainty of the POES fluxes is the scaling from the detector aperture to the bounce loss cone, which might be underestimated due to weak diffusion, as described in section 2.1. *Nesse Tyssøy et al.* [2016] showed in Figure 6 of their paper that the diffusion strength is similar between the energy channels considered in our study. However, there are clearly occasions where the diffusion strength in the lowest energy MEPED electron channel is approximately a factor of 2 higher compared with the other energy channels. Nevertheless, in most cases it seems a reasonable assumption that the measurements in the integrated flux channels will be proportionally underestimated in the case of weak diffusion, and therefore the spectral gradient should not be affected by this missing flux. Using this assumption, we now move to validate the POES fluxes using the AARDDVARK-derived fluxes.

Figure 3 shows a comparison between the AARDDVARK-reported >30 keV fluxes and the modified 10 year data set of POES-derived flux values over the range $L = 3–7$. Only the Northern Hemisphere summer period is shown in this figure, as the *Neal et al.* [2015] flux extraction approach is limited to daylit ionospheric conditions. Figure 3 (top) shows data from the summer of 2009. This was a particularly quiet period, allowing very clear visual comparisons to be made. As is apparent from this graph, during disturbed conditions with high flux levels, there is very good agreement between the AARDDVARK-extracted >30 keV flux magnitudes and those of the modified POES fluxes. However, for large periods of time the AARDDVARK-derived precipitating fluxes are smaller than the POES instrumental sensitivity floor at ~1 electron count/s (~100 electrons cm^{-2} sr^{-1} s^{-1}). In cases where the modified POES flux values were smaller than 125 cm^{-2} sr^{-1} s^{-1}, these have been set to zero and do not appear on the figure, while the AARDDVARK observations suggest they should be at least as low as ~20 electrons cm^{-2} sr^{-1} s^{-1}, which appears to be the AARDDVARK sensitivity limit.

Figure 3 (bottom) shows a scatterplot over the full period of the summers of 2005–2013, and a line fitted to all points, giving a close-to-identical relation. In this graph, the AARDDVARK fluxes seem to show more deviations to high values than the POES fluxes. These data points consist of only a few strong events, where due to the calculations to the AARDDVARK data, at very high flux values, small changes in perturbation amplitude correspond to large changes in flux, causing the AARDDVARK-derived fluxes to be less accurate in this area. In the low flux range, the limitation in the POES fluxes due to the noise floor is clearly seen also in this graph, even though all POES fluxes smaller than 185 cm^{-2} sr^{-1} s^{-1} were removed. All points shown in the graph were taken along in the fitted curve, which does not seem to be influenced significantly by either of these deviations.

Excluding solar proton events and data gaps, the cross correlation between the log_{10}(fluxes) over the Northern Hemisphere summers of 2005–2013 is 0.91. The *Neal et al.* [2015] study used observations of a VLF transmitter

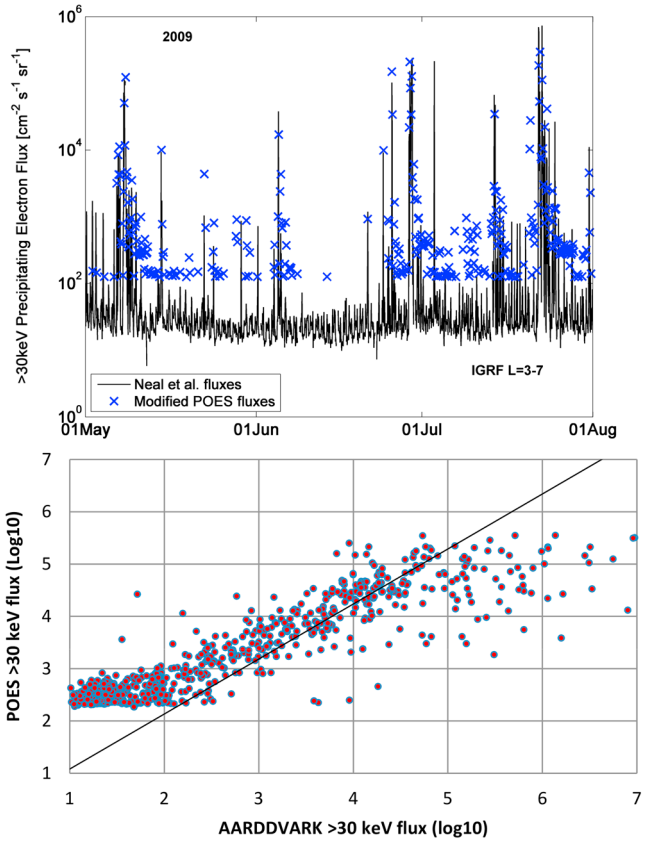

Figure 3. Comparison between the magnitude of the >30 keV precipitating electron fluxes extracted from AARDDVARK observations [*Neal et al.*, 2015] and the modified POES fluxes described in this study. (top) Summer of 2009 as a function of time; (bottom) scatterplot of 1 day resolution data over summer months (MJJ) 2005–2013, and a linear fitted curve giving $y = 1.0518x + 0.0273$.

on the east coast of North America received in northern Finland. As such, the AARDDVARK fluxes are strictly appropriate for the longitudes of the North Atlantic, while the modified POES fluxes have been zonally averaged to provide a global precipitation flux indication. Nonetheless, the cross correlation between these data series is very high, providing a validation of the modified POES fluxes. We will now consider how to apply these fluxes in order to produce multidecade estimates of precipitation into the polar atmosphere.

2.3. Comparison With Geomagnetic Activity

A visual representation of the 10 year electron precipitation data set derived from the modified POES SEM-2 measurements is shown in Figure 4, as a function of *Dst* and *L* shell (Figure 4, top) and *Ap* and *L* shell (Figure 4, bottom). The *Dst* index has been averaged to daily resolution in order to match the electron precipitation data set, and the ranges of *Dst* and *Ap* have been divided in bins. For each bin the median F_{30} and median *k* have been calculated. $Dst > 0$ nT is not considered further here in order to maintain consistency with the development of the electron precipitation model presented in section 3.

Figure 4 (left column) shows the variation of the median flux >30 keV (F_{30}). At low geomagnetic activity levels (i.e., at $Dst \sim 0$ nT and $Ap \sim 0$) the electron precipitation fluxes are low and confined to $L > 5$. As the geomagnetic disturbance levels increase the fluxes become substantially higher, as well as becoming more constrained to lower *L* shell values.

The movement of the high-precipitation flux region toward lower *L* shells as geomagnetic activity increases is consistent with the dynamical behavior of the plasmapause. *O'Brien and Moldwin* [2003] presented several models of the plasmapause expressed in various geomagnetic indices, including *Dst* and *Kp*. Since the plasmapause generally responds quickly to a geomagnetic storm, but slowly returns to normal after the storm, they found the best correlation if the geomagnetic index is integrated over a certain period before the time point

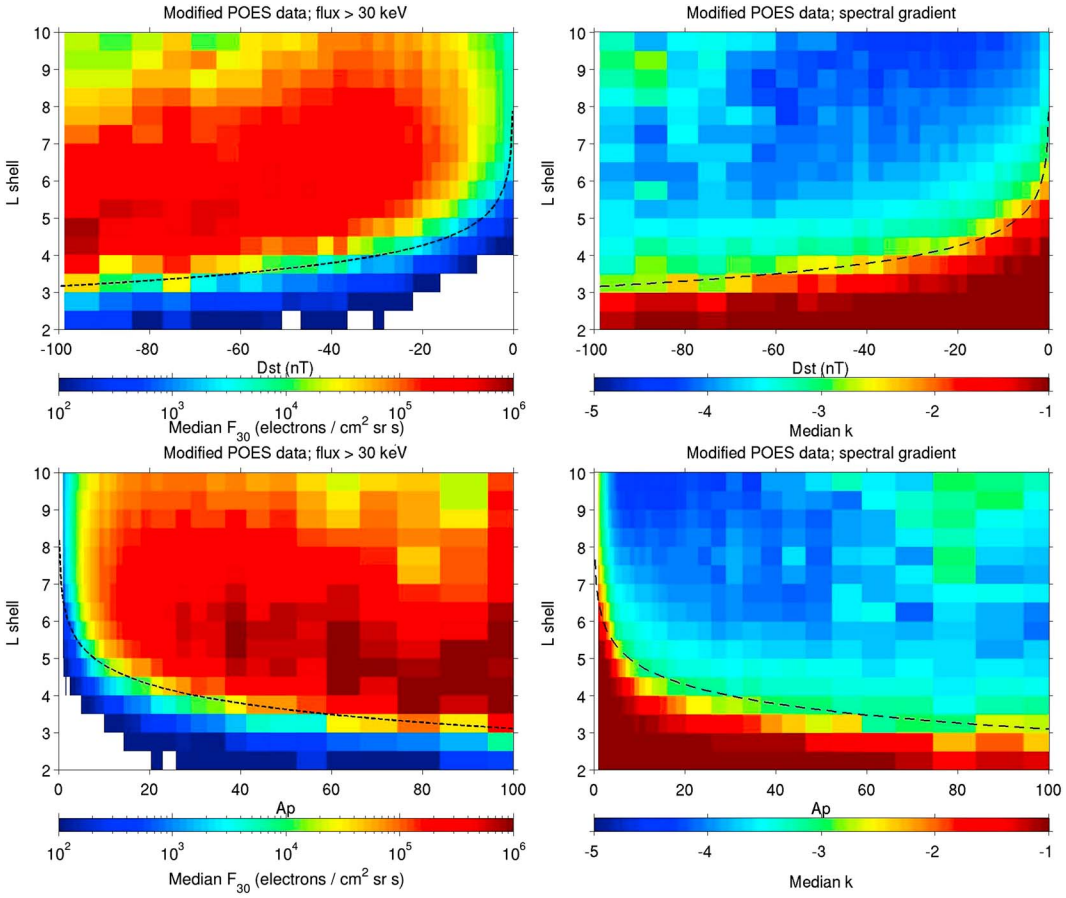

Figure 4. (left column) The median integrated flux >30 keV, F_{30}, and (right column) spectral gradient, k, as functions of (top row) L and Dst and (bottom row) L and Ap from the modified POES fluxes described in section 2. The dashed lines are the approximate plasmapause location L_{pp}, plotted as a function of $\min_{t-1,t} Dst$ and $\max_{t-1,t} Ap$, respectively.

of interest. This period is 24–36 h depending on the parameter. Their best performing models dependent on Dst and Kp have been adapted to our 1 day resolution data sets of Dst and Ap as follows:

$$L_{pp}(t) = -1.57 \log_{10} |\min...Dst| + 6.3 \quad (4)$$

$$L_{pp}(t) = -0.7430 \ln \max_{t-1,t} Ap + 6.5257 \quad (5)$$

where $\min_{t-1,t} Dst$ and $\max_{t-1,t} Ap$ indicate the minimum/maximum value of Dst/Ap of the day of interest and the previous day. The coefficients in equation (5) were obtained by fitting to the relation by definition between Kp and Ap. To show the consistency of the movement of the high-precipitation flux region toward lower L shells with the dynamical behavior of the plasmapause as geomagnetic activity increases, the approximate location of the plasmapause has been included in Figure 4 as a black dashed line.

Strong linkages between precipitation location and the plasmapause location have been reported recently [e.g., *Lichtenberger et al.*, 2013; *Simon Wedlund et al.*, 2014; *Whittaker et al.*, 2014a; *Clilverd et al.*, 2015]. The region of high precipitation flux in Figure 4 resides outside of the modeled location of the plasmapause and therefore suggests that VLF whistler mode chorus is the most dominant source of electron precipitation in the medium energy range (30–1000 keV) [*Summers et al.*, 2007; *Li et al.*, 2013; *Ni et al.*, 2014].

Figure 4 (right column) shows the median power law spectral gradient k in the electron precipitation data set. The regions of high median flux largely coincide with the regions where the median spectral gradient is steep (~−3 to −4), and those with low fluxes coincide with shallow gradients (limited to −1). The response of the spectral gradient to increased geomagnetic activity is also consistent with the behavior of the plasmapause.

3. Development of a Flux and Spectrum Model Based on Magnetic Index and *L* Shell

3.1. The Model

A model for the integrated electron flux was developed by fitting analytic expressions to the dependencies, on *Dst* or *Ap* and *L*, of the median integrated flux F_{30} and the spectral gradient *k* from the modified POES fluxes described in the previous section and shown in Figure 4.

To compensate for the movement of the plasmapause position we expressed the dependence on *L* in terms of the distance from the plasmapause, S_{pp}, defined as $S_{pp} = L - L_{pp}$. The location of the plasmapause, L_{pp}, was calculated according to equations (4) and (5). The optimal expressions for F_{30} and *k* were found manually by experimental fitting to the median observed values. In this process, most attention was paid to a good fit to the highest fluxes, because these are the main interest of the database. The coefficients of the expressions were found by least squares error regression. The resulting models for F_{30} and *k*, as functions of *Dst* and S_{pp} are

$$F_{30} = \frac{Ae^{bS_{pp}}}{\cosh(c(S_{pp} - s))} \tag{6}$$

where

$$A = 597.23(-Dst)^{1.0878}$$

$$b = 0.90109(-Dst)^{0.16200}$$

$$c = 1.0061(-Dst)^{0.19921}$$

$$s = 1/(-3.5264 \times 10^{-3} Dst + 0.65650)$$

And for the spectral gradient *k*

$$k = \frac{-1}{Ee^{-bS_{pp}} + 0.29458\cosh(0.19750(S_{pp} - 5.7000))} - 1 \tag{7}$$

where

$$E = 0.40850(-Dst)^{-0.22247}$$

$$b = 1.8375(-Dst)^{0.20602}$$

For positive *Dst*, we find that the electron fluxes are typically low and modeling these is not of prime interest in this study. Therefore, an extra clause in this model is that for any value of $Dst \geq 0$ nT, $F_{30} = 0$ electrons $cm^{-2}\ s^{-1}\ sr^{-1}$, and $k = -1$.

The models for F_{30} and *k*, as functions of *Ap* and S_{pp}, are

$$F_{30} = \frac{e^{A}}{e^{-b(S_{pp}-s)} + e^{c(S_{pp}-s)} + d} \tag{8}$$

where

$$A = 8.2091Ap^{0.16255}$$

$$b = 1.3754Ap^{0.33042}$$

$$c = 0.13334Ap^{0.42616}$$

$$s = 2.2833Ap^{-0.22990}$$

$$d = 2.7563 \times 10^{-4} Ap^{2.6116}$$

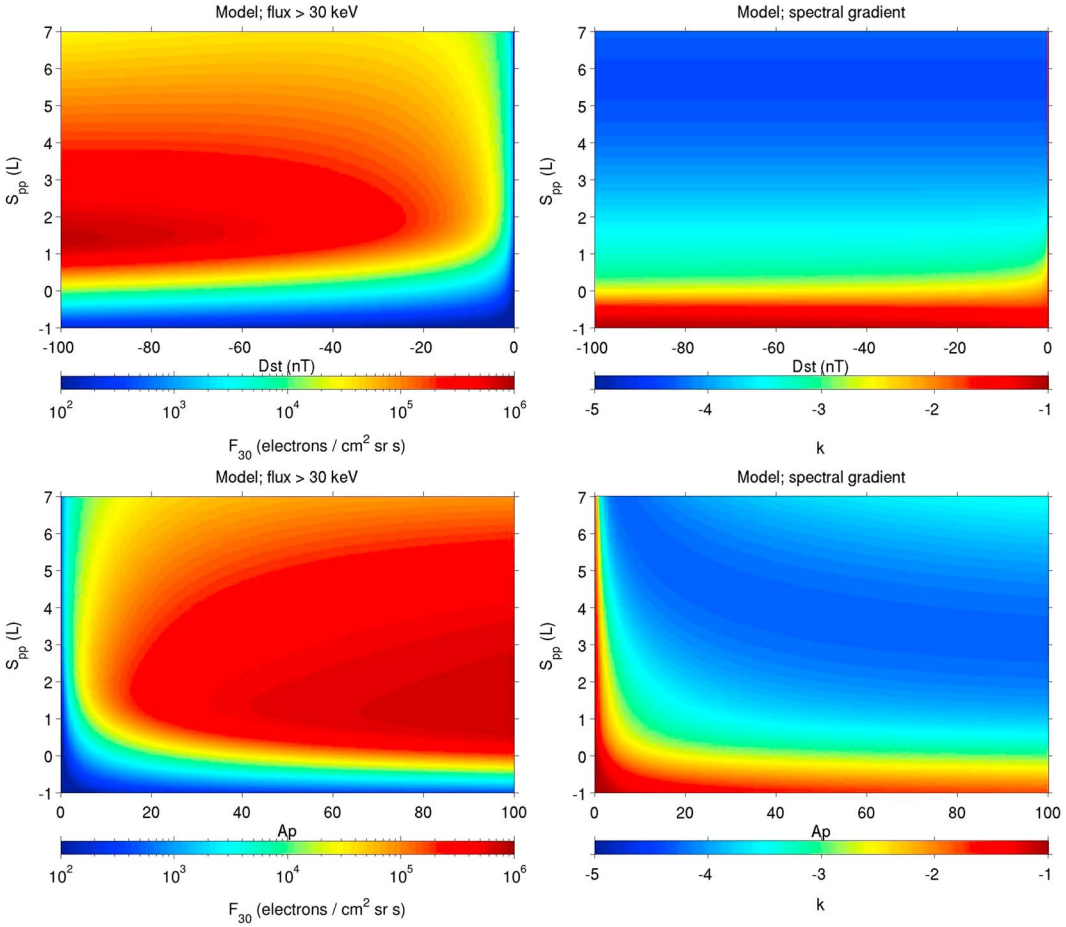

Figure 5. The modeled integrated flux >30 keV F_{30} and spectral gradient k, (top) as functions of S_{pp} and Dst and (bottom) as functions of S_{pp} and Ap.

And for the spectral gradient k

$$k = \frac{-1}{Ee^{-bS_{pp}} + 0.30450\cosh(0.20098\,(S_{pp} - s))} - 1 \tag{9}$$

where

$$E = 3.3777Ap^{-1.7038} + 0.15000$$

$$b = 3.7632Ap^{-0.16034}$$

$$s = 12.184Ap^{-0.30111}$$

The results of the above expressions as functions of Dst, Ap, and S_{pp} are shown in Figure 5. The model presented above can be used to estimate the >30 keV flux and spectral gradient k for $2 < L < 10$ and at any point in time for which the magnetic index is available.

To save space, in the following, this paper will focus mostly on the model using Ap. In order to compare the model results with the modified POES data, we calculate the F_{30} and k from Ap over the same time period and the same L values as the POES database. The results were binned as functions of Ap, and median values were calculated for every bin for comparison with Figure 4. The result is shown in Figure 6. Comparison with Figure 4 shows a good agreement with the medians of the values in each Ap/L bin of the modified POES data—a more quantitative and more complete comparison follows.

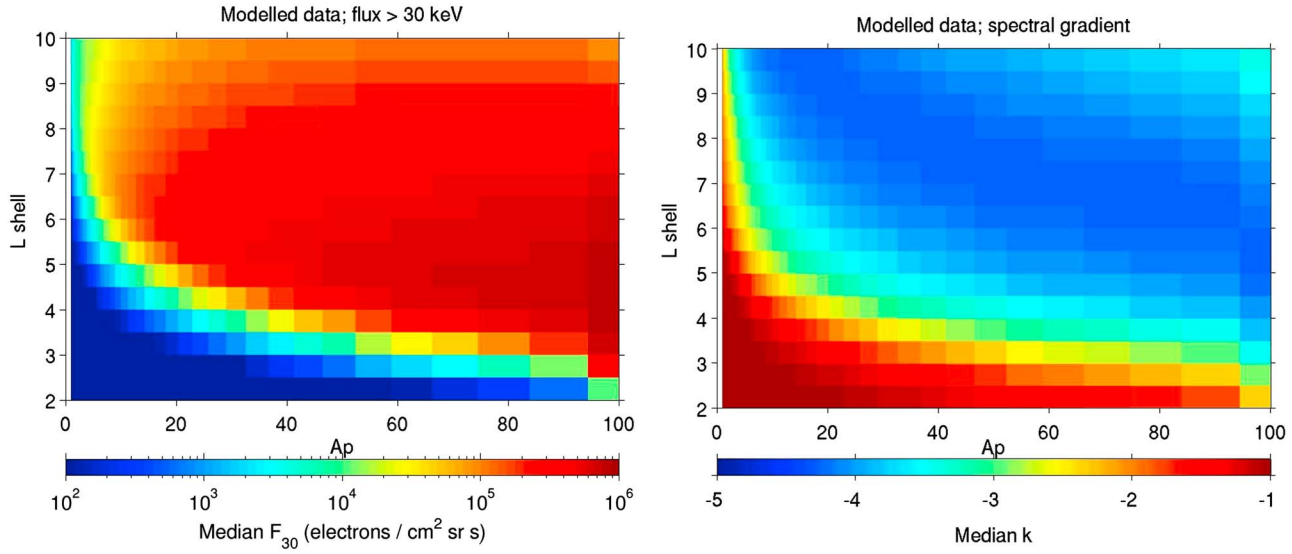

Figure 6. (left) The median modeled integrated flux >30 keV, F_{30}, and (right) spectral gradient, k, calculated over the time period of the modified POES flux observations, as functions of L and Ap.

With F_{30} and k now known, the integrated fluxes above other energy thresholds E (in keV) can now be calculated (derived from equation (2)):

$$\begin{aligned} F(E) &= F_{30}\frac{E_u^{k+1} - E^{k+1}}{E_u^{k+1} - 30^{k+1}} \qquad (k \neq -1) \\ &= F_{30}\frac{\ln E_u - \ln E}{\ln E_u - \ln 30} \qquad (k = -1), \end{aligned} \tag{10}$$

where E_u is equal to the upper energy limit of 1000 keV.

3.2. Comparison With Observations

3.2.1. Time Series Examples

Figure 7 shows a comparison of the observed (POES modified) and modeled integrated flux F_{30} over the entire POES measurement period, 2002–2012. The comparison is shown for three L values: 4.25, 5.25, and 7.75. The first two are located in the heart of the radiation belts, while $L = 7.75$ corresponds to a region in the outermost parts of the outer radiation belt. Figure 4 shows that during moderate geomagnetic disturbances (Ap between about 50 and 100), these three locations correspond roughly to the equatorward edge of the bulge in precipitating fluxes, the peak of the bulge, and its poleward slope, respectively. For the sake of clarity we have reduced the time resolution for Figure 7, presenting the 2 week median values of both POES and modeled fluxes.

3.2.2. Error Assessment

The accuracy of the model has been assessed quantitatively, and more generally in the following analysis. The error of the model in the >30 keV precipitating electron flux has been calculated as follows:

$$\epsilon_{F30}(t, L) = \log_{10} F_{30_{\text{model}}}(t, L) - \log_{10} F_{30_{\text{POES}}}(t, L).$$

The database was divided into bins according to Ap, varying almost linearly from 0 to 100 (not the same bins as used in Figures 4–6). For each of these bins, the probability density function (PDF) of ϵ_{F30} was derived for all daily data points in the respective Ap bin across all 16 L values. Points where the modified POES F_{30} was equal to zero (i.e., removed because the values were so small they were affected by the noise floor) were excluded from this determination, as these would give $\epsilon_{F30} = \infty$, while in reality the size of their error is unknown in these cases. After this, all the PDFs for the different Ap values were averaged, to obtain one overall PDF of the error ϵ_{F30}. The purpose of this averaging of separate Ap-dependent distributions is normalization, to increase the visibility of the disturbed time results. If the PDF of all data were calculated at once, the result would be dominated by the quiet-time results, as they are the most common situation in the data. Using the averaging, the behavior for different levels of disturbance are equally represented in the end result.

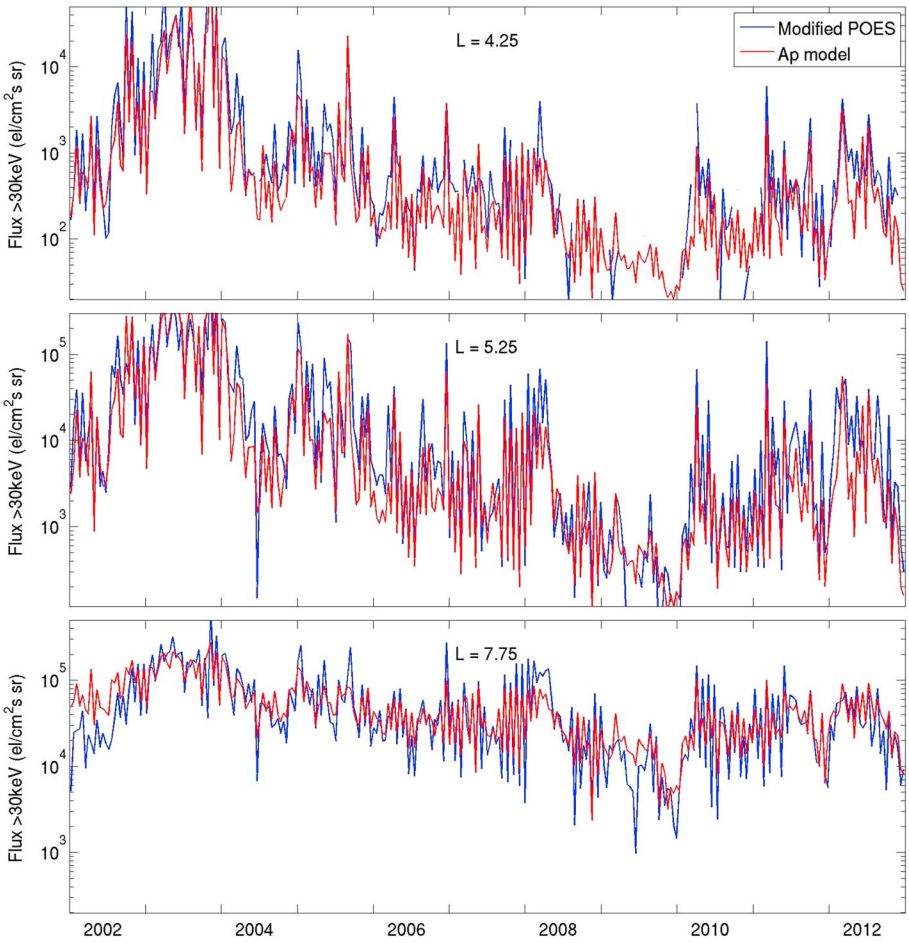

Figure 7. The observed (modified POES, blue line) and modeled (*Ap* model, red line) integrated precipitating >30 keV flux over the entire POES SEM-2 measurement period, at three IGRF *L* shells: 4.25, 5.25, and 7.75. For clarity, all values shown are medians over 14 days.

Figure 8 (top) shows the overall PDF for F_{30} (blue line). This figure indicates the PDF is roughly Gaussian, distributed around ∼−0.01, with a standard deviation of 0.69.

In order to extend the error analysis to involve the spectral gradient, the integrated fluxes >100 keV and >300 keV (F_{100} and F_{300}), were additionally analyzed. The modeled values were calculated from the modeled F_{30} and k using equation (10) with $E = 100$ keV/300 keV and $E_u = 1000$ keV. The same approach was applied to the F_{30} and k values obtained from the modified POES data set, resulting in virtual measured values of F_{100} and F_{300}. Similarly as for ϵ_{F30}, these were used to calculate the errors ϵ_{F100} and ϵ_{F300}, but these errors are now influenced by a combination of the modeling accuracies of both F_{30} and k. The green and red lines in the upper graph of Figure 8 show the PDFs of ϵ_{F100} and ϵ_{F300}. They are also roughly Gaussian, with means, respectively, −0.01 and 0.02 and standard deviations 0.63 and 0.71. The errors ϵ_{F30} and ϵ_{F300} of the *Dst*-based model are also included (dashed lines), calculated equivalently as that of the *Ap* model, averaging PDFs for different *Dst* bins. Their means are, respectively, −0.05 and 0.07, and the standard deviations are 0.90 and 0.65.

The graph shows that errors of up to about a factor 10 (both ways) are fairly common in all fluxes. This is equal to the general spread of measured values within each bin of *Dst*/*Ap* and *L*, and therefore indicates the limitation of the predicting ability of these parameters. Partly, this variation can be due to the zonal averaging of the data, and a better performance still can be expected when MLT dependence is included in later versions of the models.

In order to show the performance of both models dependent on geomagnetic activity, the means and standard deviations of the PDFs for the different *Ap* and *Dst* bins are shown in Figure 8 (middle). Only results for bins containing more than one time sample (=16 values) are shown. Here it is seen that the standard deviations of

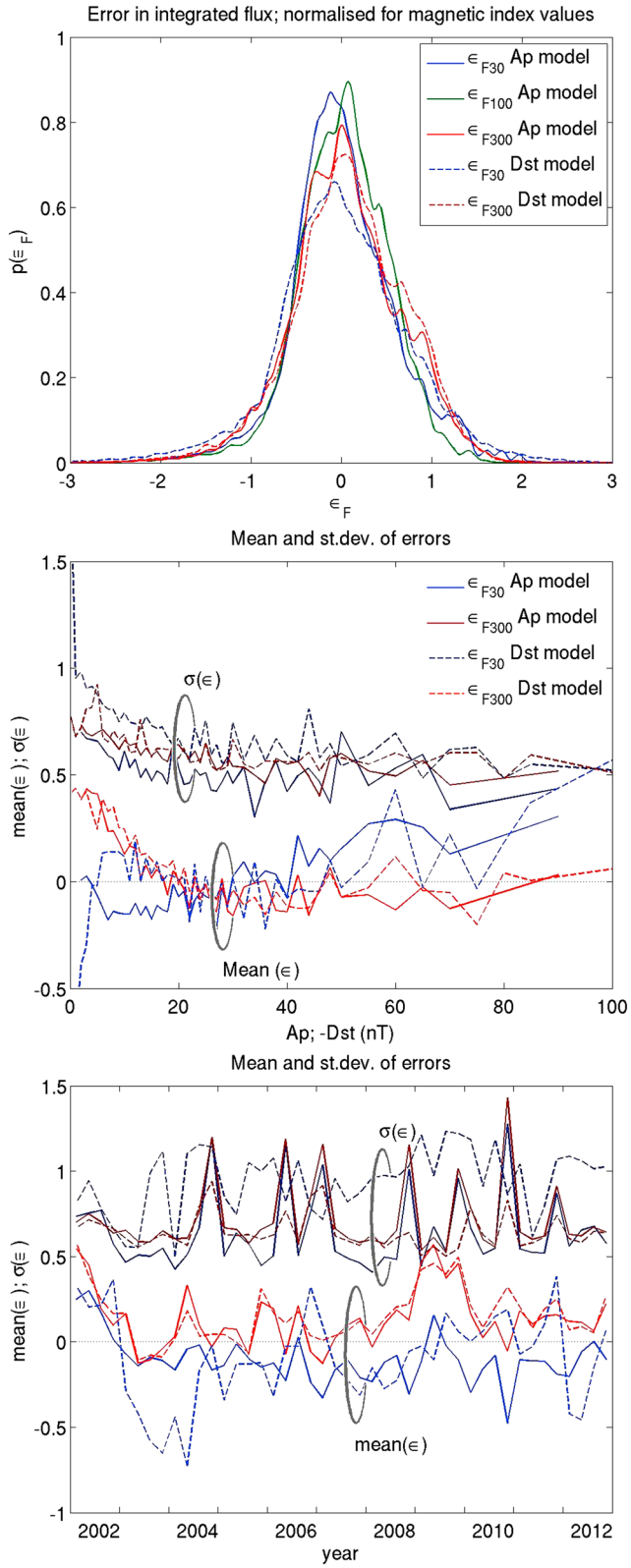

Figure 8. (top) The PDF of the error of the *Ap* model, for three energy channels, and for the *Dst* model for two energy channels; see text for details. (middle) The mean error (red and blue solid and dashed lines) and standard deviation of the error, σ, (same as the mean but darker red and blue coloring) of both models, from the distributions for the different *Dst*/*Ap* bins. (bottom) The means and standard deviations as functions of time, with 3 month resolution. In Figures 8 (top) and 8 bottom, all distributions have been averaged from the PDFs for different *Dst*/*Ap* bins.

F_{30} are fairly constant over the range, and the means fluctuate around zero, indicating a stable performance of the models over most of the range.

For ϵ_{F300}, the mean errors are found to be relatively large in quiet conditions (low *Ap* and |*Dst*|). This overestimation of fluxes at high energies is due to overestimations of the spectral gradient in quiet conditions. As shown before, quiet conditions are cases where the fluxes tend to be low (see, e.g., Figure 4) and therefore of less interest in this study. In addition, it was shown that the measurement of low fluxes in the POES campaign are relatively inaccurate due to noise. For both reasons, the fitting procedure of equations (7) and (9) was aimed more at the higher fluxes than the lower, which is the reason for the poorer prediction of the spectral index in quiet conditions.

In order to show the performance of both models as functions of solar cycle phase, the error distributions were also calculated for 3 month periods over the time period of the database. Also, these were derived by averaging the error distributions for the different *Ap*/*Dst* bins. Note, however, that any data for high disturbance levels were only measured around solar maximum, causing other results to represent only data for lower disturbance (e.g., during 2006–2011 only $Ap < 50$ and in 2009 only $Ap < 20$). The resulting means and standard deviations of these are shown in Figure 8 (bottom). Here it is seen that for the *Ap* model, the error for F_{30} is stable over the solar cycle period. The *Dst* model tends to underestimate F_{30} just after the solar maximum around 2003, while it performs better during other periods. This underestimation is systematic, as it was seen at all disturbance levels during that period (not shown). The already observed overestimations of F_{300} for both models seem to increase at solar minimum; however, this is caused by biasing toward lower disturbance levels due to the lack of other data, as mentioned above. The standard deviations are all fairly independent of solar cycle phase.

4. Atmospheric Ionization Rates From the Precipitation Model

Using the precipitation model described in section 3 and the spectrum estimate described in section 2, it is now possible to calculate an electron energy-flux spectrum for any *Dst*/*Ap* index and *L* shell combination. Further, these spectra can be used in calculation of altitude-dependent atmospheric ionization rates. To demonstrate this, we have calculated a set of ionization rates for years 2002–2012 from both precipitation models presented above using a parameterization of electron impact ionization by *Fang et al.* [2010]. For comparison, the ionization rates were also calculated from the flux spectra resulting from the modified POES data set over the same period. The energy range of the spectrum was set at 30–1000 keV, with 168 logarithmically spaced grid points.

A representation of the atmosphere, as needed for the ionization rate calculation, was created using the NRLMSISE-00 model [*Picone et al.*, 2002]. Note that the rates were calculated on a fixed atmospheric pressure grid, and the altitude grid shown in the following figures is approximated. Although the rates were calculated with 1 day temporal resolution, for clarity we present 14 day median values in the figures.

Figure 9 shows the altitude-dependent ionization rates at *L* shell 5.25 according to both models and to the modified POES data. Zero values are shown as blanks in these graphs, while values between 0 and 0.01 cm^{-3} s^{-1} are dark blue. This figure shows that the main part of the ionization due to the energy range considered in this paper is between 70 and 110 km altitude, while the rates decrease rapidly at altitudes below and above. The peak of the ionization, at about 90 km, is caused partly by the 30 keV lower limit of electron spectrum energy. The lower altitude limit of the ionization of this energy range is seen at about 55 km (Figure 9), because the electrons with highest spectrum energy (1000 keV) can not penetrate to altitudes below this height [e.g., *Turunen et al.*, 2009, Figure 3].

It should be noted that the ionization profile shown here is only that caused by electrons in the energy range 30–1000 keV. The profiles due to electrons of lower and higher energies will overlap this profile, and show maximum ionization at higher and lower altitudes, respectively. The altitude range which is dominated by ionization from electrons in the energy range considered in this paper, and where the profile of Figure 9 can therefore be assumed to be close to the total ionization profile, is between about 60 and 95 km.

Comparing the graphs in Figure 9, the ionization rates according to both models generally agree well with those according to the modified POES data. Also, here, it can be seen that in the strong disturbance period of 2003, the *Dst* model slightly underestimates the ionization. Otherwise, the most obvious differences between the three results are in the low ionization area and the zero values indicated as blanks in the graphs. The POES

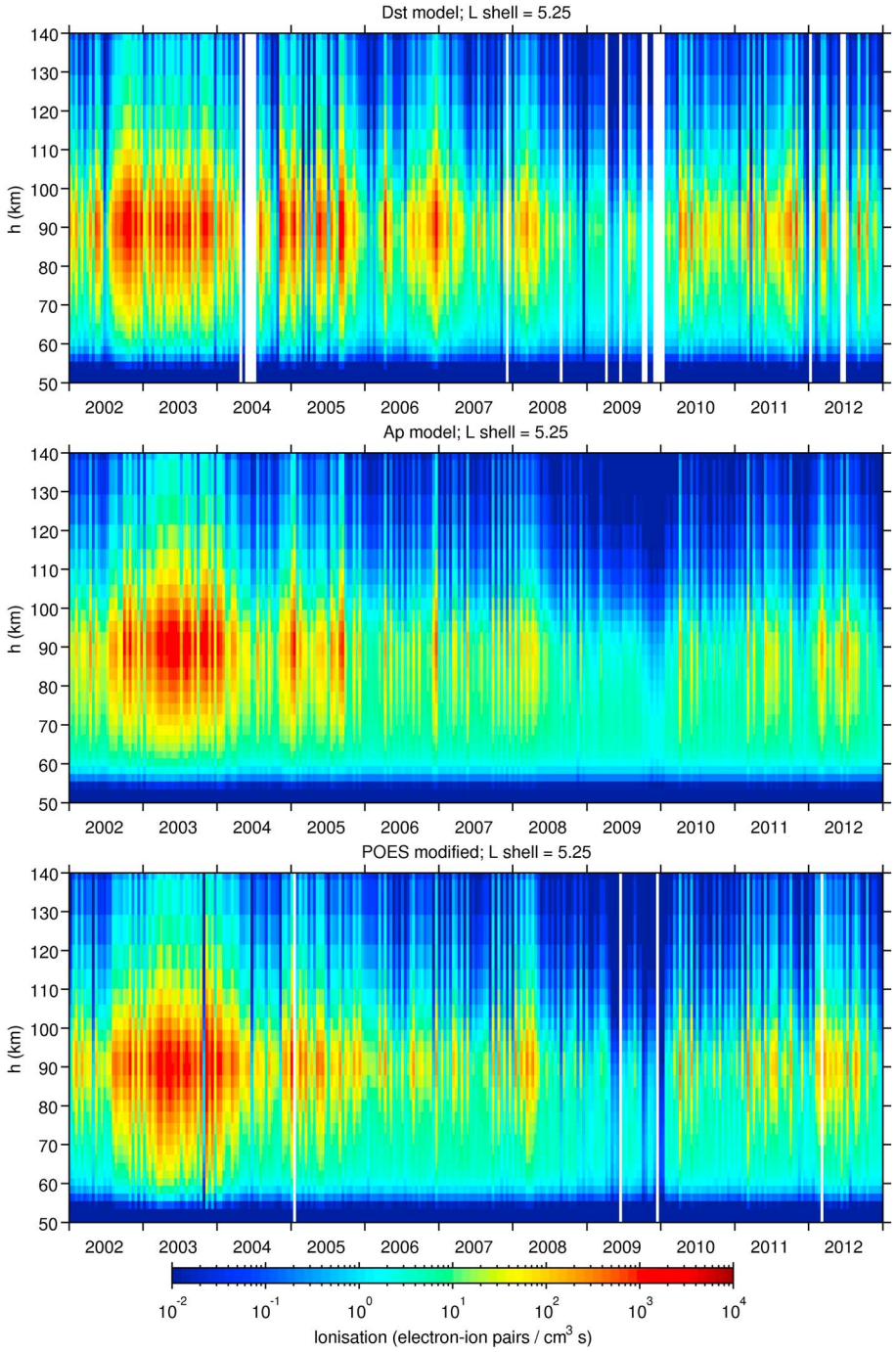

Figure 9. Ionization rates due to 30–1000 keV radiation belt electron precipitation from 2002 to 2012 at *L* shell 5.25, according to (top) the *Dst* model, (middle) the *Ap* model, and (bottom) POES observations.

ionizations are occasionally zero, in case of low or removed fluxes (see section 2.1). The *Dst* model gives zero even more often, in cases of positive *Dst* values. The *Ap* model remains consistently positive in all these cases.

Figure 10 presents the *L* shell distribution of the ionization rates at 89 km altitude, near the peak of ionization of this energy range. Large variability is seen with respect to the *L* shell, with the highest ionization rates reaching 2×10^3 cm^{-3} s^{-1}. The main region with large ionization values lie between *L* shells 5 and 10, i.e., including the heart of the radiation belts at the latitudes most likely to be significantly impacted by substorms

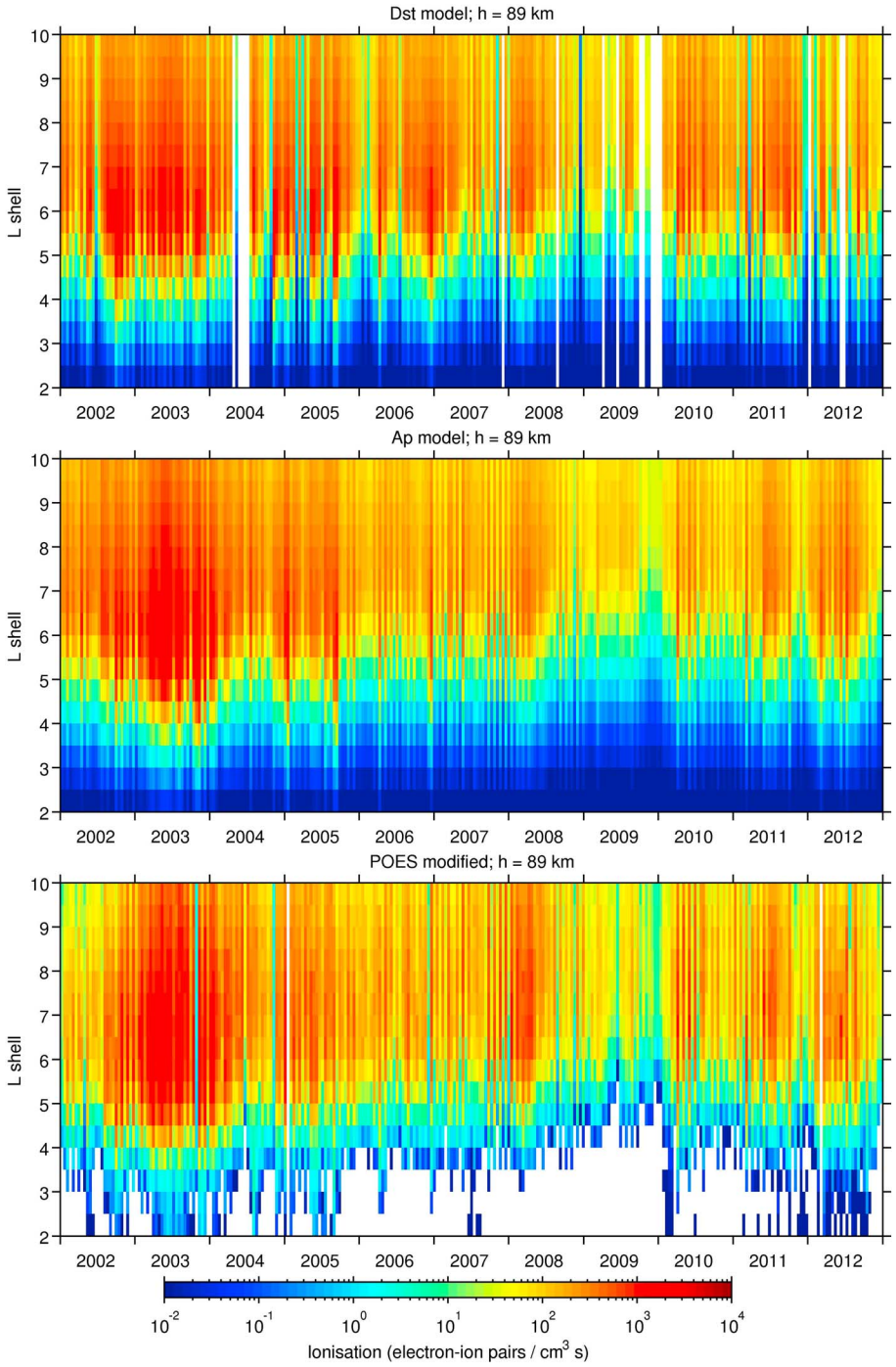

Figure 10. Ionization rates due to 30–1000 keV radiation belt electron precipitation at 89 km altitude in 2002–2012, according to (top) the *Dst* model, (middle) the *Ap* model, and (bottom) POES observations.

[*Cresswell-Moorcock et al.*, 2013]. At the lower *L* shells ($L < 5$) the ionization rates are substantially smaller and indicate a more infrequent, event-like behavior compared to that seen at higher *L* shells.

Comparing the graphs in Figure 10, again the *Dst* model is seen to slightly underestimate the ionization in 2003. Zero values occur in the POES ionizations often for low *L* values (inside the plasmaspause footprint), while neither model gives zero ionization there.

In both Figures 9 and 10, the ionization rates vary in time by more than 4 orders of magnitude. Following the variations in the solar and geomagnetic activity, 2003 has the highest ionization levels across the year while

2009 has the lowest. In May–June 2004, in the midst of an otherwise generally high ionization period, the rates are substantially smaller; this variation is consistent with observations of radiation belt variability over this time [*Rodger et al.*, 2016]. Note that using the model proposed here the ionization rates due to EEP can now also be calculated during the SPE periods (e.g., October–November 2003, December 2006, and early 2012), when any calculations based on POES data would suffer from serious proton contamination (see the discussion in *Rodger et al.* [2013, section 2.3] and *Neal et al.* [2015, section 6]). The ionization predicted by the model during SPEs would be equal to that during the same levels of disturbance outside of SPEs, assuming that the SPE would not affect this precipitation. Obviously, the additional electron precipitation due to the SPE itself is not predicted by the models.

A more detailed analysis of the variability of the ionization in this data set is outside the scope of this paper. A discussion on the longer-term variability of the ionization rates described by the *Ap* model and examples of resulting atmospheric response are given by *Matthes et al.* [2016].

5. Evaluation

5.1. Intercomparison of the Two Models

In case the user intends to apply the EEP models presented in this paper to their own atmospheric model, or to any other purpose, a choice between the two models presented in section 3.1 (*Dst*- and *Ap*-dependent model) can be made. Both models perform almost equally well, so that the choice can simply depend on preference or suitability of either of the magnetic indices for the intended application. However, each of the two models has small advantages and disadvantages over the other.

The *Ap* model (equations (6) and (7)) has the advantage over the *Dst* model that its performance is a bit better, see the standard deviation of the modeled flux in Figure 8 (top). This performance is independent of solar cycle phase, as seen in Figure 8 (bottom). Furthermore, if a long-term database is needed, the index *Ap* has the advantage of being available further back into the past than *Dst* (from 1932).

The *Dst* model (equations (8) and (9)), even though its overall error standard deviation is slightly less good, has the potential advantage of a higher time resolution. The index *Dst* is available at a time resolution of 1 h. Since *Dst* is, more than *Ap*, linked to dynamics of the inner magnetospheric electric field which causes erosion of the plasmasphere [*O'Brien and Moldwin*, 2003], it can be expected that this index responds quickly to dynamics of the plasmapause. It has been tested using POES observations (not shown in this paper) that the *Dst* model performs still almost as well at a time resolution of 3 h as it does at 1 day: the mean error stays close to zero and the standard deviation only slightly increases. A disadvantage of the *Dst*-dependent model is the underestimation of the flux just after solar maximum. Another disadvantage may be the zero flux values which the *Dst* model can give during quiet conditions when $Dst \geq 0$ nT, and which may not be desired in some applications.

5.2. Limitations of the Models

The precipitation models presented above and the ionization rates based on them have certain limitations.

The presented ionization rates are zonally averaged and have no information on longitudinal variability of the precipitation. This variability may explain some of the spread of the error shown in Figure 8. We have applied this approach in the first version of the electron precipitation model because of the large size of the POES data set. In future it may be possible to retain the information on the magnetic local time coverage of the observations, which could be used to obtain some information on the longitudinal variability of the precipitating fluxes. This, however, is a significant task and therefore the ionization rates from the model currently represent the average longitudinal precipitation. Still, they show good agreement with the AARDDVARK measurements which have much less longitudinal averaging.

Furthermore, the measurements are relatively inaccurate for low flux levels. First, weak diffusion may cause the electrons to be located near the edge of the bounce loss cone and missed by the detector, causing underestimations (although the AARDDVARK validation shows that this error is not very large). Second, the low flux measurements are subject to noise, causing overestimations (even after the precautions described in section 2.1). Third, the fitting of the models to the observations was mainly aimed at the higher flux levels. Because of all these reasons, the models will not be very accurate for low flux levels, as was indeed seen in Figure 8. However, since the purpose of the models is mainly predicting the larger flux levels, this is not a cause of great concern.

Finally, we have focused these models on medium energy EEP in the energy range 30–1000 keV, which will likely be dominated by precipitation due to chorus waves. We plan for mechanisms working at higher energies to be included in an updated version of the geomagnetic index driven electron precipitation model in the future. As not all precipitation mechanisms can be presently included, it should be noted that the ionization rates based on the precipitation model remain an underestimation of the total ionization from energetic electron precipitation into the atmosphere.

6. Conclusions

We have developed a precipitation model for radiation belt energetic electron precipitation in the energy range 30–1000 keV, which can be used to calculate the first ever >80 year long atmospheric ionization rate data set. The EEP model is based on available observational data from satellites, the plasmasphere structure and geomagnetic activity. The satellite precipitation measurements have been partly validated through comparison with electron precipitation measurements from the AARDDVARK network.

Results from the EEP model, which uses *Dst* or *Ap* index to determine the varying geomagnetic activity levels, compare well with processed observational data over the period of 2002–2012.

The main impact from the ionization from EEP is focused on the mesosphere-lower thermosphere altitudes (70–110 km), with the lower limit of the ionization located at about 55 km altitude. This lower limit is a result of the limitation of the energy range in this first version of the EEP model presented here. Future work will focus on adding subsequent precipitation mechanisms, which will extend the range of impact altitudes, and bring us closer to being able to estimate the total EEP impact into the atmosphere. While the current ionization rates will enable us to make the first long-term simulations of EEP impacts on the atmosphere and climate, we note that these remain an underestimation of the total EEP ionization.

To enable long-term studies of EEP impact on the atmosphere, the ionization rates calculated from the EEP model results are available for the scientific community for use with chemistry-climate models, at http://solarisheppa.geomar.de/cmip6. A discussion on the ionization rates and their variability over the data set duration has been published separately [*Matthes et al.*, 2016].

Acknowledgments

We thank the Academy of Finland for supporting this research: M. van de Kamp and A. Seppälä were supported by projects 258165, 265005, and 292806 (CLASP: Climate and Solar Particle Forcing), P. T. Verronen was supported by the project 276926 (SECTIC: Sun-Earth Connection Through Ion Chemistry). M. A. Clilverd was supported by the Natural Environmental Research Council grant NE/J008125/1. A. Seppälä, M. A. Clilverd, C. J. Rodger, and P. T. Verronen would like to thank the International Space Science Institute (ISSI), Bern, Switzerland for supporting the "Quantifying Hemispheric Differences in Particle Forcing Effects on Stratospheric Ozone" team (Leader: D. R. Marsh). We would like to thank the geomagnetic data suppliers and the World Data Center for Geomagnetism, Kyoto, for making the *Dst* index data available via http://wdc.kugi.kyoto-u.ac.jp. The NOAA/POES data used in this study were made available by the National Oceanic and Atmospheric Administration. AARDDVARK data are available from the AARDDVARK Konsortia (see http://www.physics.otago.ac.nz/space/AARDDVARK_homepage.htm). Other data presented in the paper are available from the corresponding author (annika.seppala@fmi.fi).

References

Andersson, M. E., P. T. Verronen, C. J. Rodger, M. A. Clilverd, and A. Seppälä (2014), Missing driver in the Sun-Earth connection from energetic electron precipitation impacts mesospheric ozone, *Nat. Commun.*, *5*, 5197, doi:10.1038/ncomms6197.

Baumgaertner, A. J. G., P. Jöckel, and C. Brühl (2009), Energetic particle precipitation in ECHAM5/MESSy1 Part 1: Downward transport of upper atmospheric NOx produced by low energy electrons, *Atmos. Chem. Phys.*, *9*, 2729–2740.

Baumgaertner, A. J. G., A. Seppälä, P. Jöckel, and M. A. Clilverd (2011), Geomagnetic activity related NOx enhancements and polar surface air temperature variability in a chemistry climate model: Modulation of the NAM index, *Atmos. Chem. Phys.*, *11*, 4521–4531, doi:10.5194/acp-11-4521-2011.

Borovsky, J. E., and M. H. Denton (2006), Differences between CME-driven storms and CIR-driven storms, *J. Geophys. Res.*, *111*, A07S08, doi:10.1029/2005JA011447.

Callis, L. B. (1997), Odd nitrogen formed by energetic electron precipitation as calculated from TIROS data, *Geophys. Res. Lett.*, *24*(24), 3237–3240.

Callis, L. B., R. E. Boughner, D. N. Baker, R. A. Mewaldt, J. B. Blake, R. S. Selesnick, J. R. Cummings, M. Natarajan, G. M. Mason, and J. E. Mazur (1996), Precipitating electrons: Evidence for effects on mesospheric odd nitrogen, *Geophys. Res. Lett.*, *23*, 1901–1904.

Carpenter, D. L. (1963), Whistler evidence of a 'knee' in the magnetospheric ionization density profile, *J. Geophys. Res.*, *68*, 1675–1682.

Carpenter, D. L., and R. R. Anderson (1992), An ISEE/whistler model of equatorial electron density in the magnetosphere, *J. Geophys. Res.*, *97*, 1097–1108.

Carson, B. R., C. J. Rodger, and M. A. Clilverd (2013), POES satellite observations of EMIC-wave driven relativistic electron precipitation during 1998–2010, *J. Geophys. Res. Space Physics*, *118*, 232–243, doi:10.1029/2012JA017998.

Clilverd, M. A., C. J. Rodger, R. J. Gamble, T. Ulich, T. Raita, A. Seppälä, J. C. Green, N. R. Thomson, J.-A. Sauvaud, and M. Parrot (2010), Ground-based estimates of outer radiation belt energetic electron precipitation fluxes into the atmosphere, *J. Geophys. Res.*, *115*, A12304, doi:10.1029/2010JA015638.

Clilverd, M. A., R. Duthie, R. Hardman, A. T. Hendry, C. J. Rodger, T. Raita, M. Engebretson, M. R. Lessard, D. Danskin, and D. K. Milling (2015), Electron precipitation from EMIC waves: A case study from 31 May 2013, *J. Geophys. Res. Space Physics*, *120*, 3618–3631, doi:10.1002/2015JA021090.

Codrescu, M. V., T. J. Fuller-Rowell, R. G. Roble, and D. S. Evans (1997), Medium energy particle precipitation influences on the mesosphere and lower thermosphere, *J. Geophys. Res.*, *102*(A9), 19,977–19,987.

Cresswell-Moorcock, K., C. J. Rodger, A. Kero, A. B. Collier, M. A. Clilverd, I. Häggström, and T. Pitkänen (2013), A reexamination of latitudinal limits of substorm-produced energetic electron precipitation, *J. Geophys. Res. Space Physics*, *118*, 6694–6705, doi:10.1002/jgra.50598.

Evans, D. S., and M. S. Greer (2004), Polar orbiting environmental satellite space environment monitor—2: Instrument descriptions and archive data documentation, NOAA Tech. Mem. 1.4, Space Environ. Cent., Boulder, Colo.

Fang, X., C. E. Randall, D. Lummerzheim, W. Wang, G. Lu, S. C. Solomon, and R. A. Frahm (2010), Parameterization of monoenergetic electron impact ionization, *Geophys. Res. Lett.*, *37*, L22106, doi:10.1029/2010GL045406.

Funke, B., M. López-Puertas, G. Stiller, and T. von Clarmann (2014a), Mesospheric and stratospheric NOy produced by energetic particle precipitation during 2002–2012, *J. Geophys. Res. Atmos.*, *119*, 4429–4446, doi:10.1002/2013JD021404.

Funke, B., M. López-Puertas, L. Holt, C. E. Randall, G. Stiller, and T. von Clarmann (2014b), Hemispheric distributions and interannual variability of NOy produced by energetic particle precipitation in 2002–2012, *J. Geophys. Res. Atmos.*, *119*, 13,565–13,582, doi:10.1002/2014JD022423.

Hardman, R., M. A. Clilverd, C. J. Rodger, J. B. Brundell, R. Duthie, R. H. Holzworth, I. R. Mann, D. K. Milling, and E. Macusova (2015), A case study of electron precipitation fluxes due to plasmaspheric hiss, *J. Geophys. Res. Space Physics*, *120*, 6736–6748, doi:10.1002/2015JA021429.

Jackman, C. H., et al. (2008), Short- and medium-term atmospheric constituent effects of very large solar proton events, *Atmos. Chem. Phys.*, *8*(3), 765–785, doi:10.5194/acp-8-765-2008.

Jackman, C. H., D. R. Marsh, F. M. Vitt, R. R. Garcia, C. E. Randall, E. L. Fleming, and S. M. Frith (2009), Long-term middle atmospheric influence of very large solar proton events, *J. Geophys. Res.*, *114*, D11304, doi:10.1029/2008JD011415.

Lam, M. M., R. B. Horne, N. P. Meredith, S. A. Glauert, T. Moffat-Griffin, and J. C. Green (2010), Origin of energetic electron precipitation >30 keV into the atmosphere, *J. Geophys. Res.*, *115*, A00F08, doi:10.1029/2009JA014619.

Li, W., B. Ni, R. M. Thorne, J. Bortnik, J. C. Green, C. A. Kletzing, W. S. Kurth, and G. B. Hospodarsky (2013), Constructing the global distribution of chorus wave intensity using measurements of electrons by the POES satellites and waves by the Van Allen Probes, *Geophys. Res. Lett.*, *40*, 4526–4532, doi:10.1002/grl.50920.

Lichtenberger, J., et al. (2013), The plasmasphere during a space weather event: First results from the PLASMON project, *J. Space Weather Space Clim.*, *3*, A3, doi:10.1051/swsc/2013045.

Lu, H., M. A. Clilverd, A. Seppälä, and L. L. Hood (2008), Geomagnetic perturbations on stratospheric circulation in late winter and spring, *J. Geophys. Res.*, *113*, D16106, doi:10.1029/2007JD008915.

Matthes, K., et al. (2016), Solar forcing for CMIP6 (v3.1), *Geosci. Model Dev. Discuss.*, doi:10.5194/gmd-2016-91.

Mayaud, P. N. (1980), *Derivation, Meaning, and Use of Geomagnetic Indices, Geophys. Monogr. Ser.*, vol. 22, AGU, Washington, D. C.

McIlwain, C. E. (1961), Coordinates for mapping the distribution of magnetically trapped particles, *J. Geophys. Res.*, *66*(11), 3681–3691, doi:10.1029/JZ066i011p03681.

Neal, J. J., C. J. Rodger, and J. C. Green (2013), Empirical determination of solar proton access to the atmosphere: Impact on polar flight paths, *Space Weather*, *11*, 420–433, doi:10.1002/swe20066.

Neal, J. J., C. J. Rodger, M. A. Clilverd, N. R. Thomson, T. Raita, and Th. Ulich (2015), Long-term determination of energetic electron precipitation into the atmosphere from AARDDVARK subionospheric VLF observations, *J. Geophys. Res. Space Physics*, *120*, 2194–2211, doi:10.1002/2014JA020689.

Nesse Tyssøy, H., and J. Stadsnes (2015), Cutoff latitude variation during solar proton events: Causes and consequences, *J. Geophys. Res. Space Physics*, *120*, 553–563, doi:10.1002/2014JA020508.

Nesse Tyssøy, H., M. I. Sandanger, L.-K. G. Ødegaard, J. Stadsnes, A. Aasnes, and A. E. Zawedde (2016), Energetic electron precipitation into the middle atmosphere—Constructing the loss cone fluxes from MEPED POES, *J. Geophys. Res. Space Physics*, *120*, 5693–5707, doi:10.1002/2016JA022752.

Ni, B., W. Li, R. M. Thorne, J. Bortnik, J. C. Green, C. A. Kletzing, W. S. Kurth, G. B. Hospodarsky, and M. de Soria-Santacruz Pich (2014), A novel technique to construct the global distribution of whistler mode chorus wave intensity using low-altitude POES electron data, *J. Geophys. Res. Space Physics*, *119*, 5685–5699, doi:10.1002/2014JA019935.

O'Brien, T. P., and M. B. Moldwin (2003), Empirical plasmapause models from magnetic indices, *Geophys. Res. Lett.*, *30*(4), 1152, doi:10.1029/2002GL016007.

Picone, J. M., A. E. Hedin, D. P. Drob, and A. C. Aikin (2002), NRLMSISE-00 empirical model of the atmosphere: Statistical comparisons and scientific issues, *J. Geophys. Res.*, *107*(A12), 1468, doi:10.1029/2002JA009430.

Randall, C. E., V. L. Harvey, C. S. Singleton, S. M. Bailey, P. F. Bernath, M. Codrescu, H. Nakajima, and J. M. Russell III (2007), Energetic particle precipitation effects on the Southern Hemisphere stratosphere in 1992–2005, *J. Geophys. Res.*, *112*, D08308, doi:10.1029/2006JD007696.

Randall, C. E., V. L. Harvey, L. A. Holt, D. R. Marsh, D. E. Kinnison, B. Funke, and P. F. Bernath (2015), Simulation of energetic particle precipitation effects during the 2003–2004 Arctic winter, *J. Geophys. Res. Space Physics*, *120*, 5035–5048, doi:10.1002/2015JA021196.

Rodger, C. J., M. A. Clilverd, J. C. Green, and M. M. Lam (2010a), Use of POES SEM-2 observations to examine radiation belt dynamics and energetic electron precipitation into the atmosphere, *J. Geophys. Res.*, *115*, A04202, doi:10.1029/2008JA014023.

Rodger, C. J., B. R. Carson, S. A. Cummer, R. J. Gamble, M. A. Clilverd, J-A. Sauvaud, M. Parrot, J. C. Green, and J.-J. Berthelier (2010b), Contrasting the efficiency of radiation belt losses caused by ducted and non-ducted whistler mode waves from ground-based transmitters, *J. Geophys. Res.*, *115*, A12208, doi:10.1029/2010JA015880.

Rodger, C. J., M. A. Clilverd, A. J. Kavanagh, C. E. J. Watt, P. T. Verronen, and T. Raita (2012), Contrasting the responses of three different ground-based instruments to energetic electron precipitation, *Radio Sci.*, *47*, RS2021, doi:10.1029/2011RS004971.

Rodger, C. J., A. J. Kavanagh, M. A. Clilverd, and S. Marple (2013), Comparison between POES energetic electron precipitation observations and riometer absorptions: Implications for determining true precipitation fluxes, *J. Geophys. Res. Space Physics*, *118*, 7810–7821, doi:10.1002/2013JA019439.

Rodger, C. J., K. Cresswell-Moorcock, and M. A. Clilverd (2016), Natures grand experiment: Linkage between solar wind speeds, substorms, and the radiation belts, *J. Geophys. Res. Space Physics*, *121*, 171–189, doi:10.1002/2015JA021537.

Rozanov, E., M. Calisto, T. Egorova, T. Peter, and W. Schmutz (2012), Influence of the precipitation energetic particles on atmospheric chemistry and climate, *Surv. Geophys.*, *33*, 483–501, doi:10.1007/s10712-012-9192-0.

Seppälä, A., and M. A. Clilverd (2014), Energetic particle forcing of the Northern Hemisphere winter stratosphere: Comparison to solar irradiance forcing, *Front. Phys.*, *2*, 25, doi:10.3389/fphy.2014.00025.

Seppälä, A., C. E. Randall, M. A. Clilverd, E. V. Rozanov, and C. J. Rodger (2009), Geomagnetic activity and polar surface air temperature variability, *J. Geophys. Res.*, *114*, A10312, doi:10.1029/2008JA014029.

Seppälä, A., H. Lu, M. A. Clilverd, and C. J. Rodger (2013), Geomagnetic activity signatures in wintertime stratosphere wind, temperature, and wave response, *J. Geophys. Res. Atmos.*, *118*, 2169–2183, doi:10.1002/jgrd.50236.

Seppälä, A., K. Matthes, C. E. Randall, and I. A. Mironova (2014), What is the solar influence on climate? Overview of activities during CAWSES-II, *Prog. Earth Planet. Sci.*, *1*, 24, doi:10.1186/s40645-014-0024-3.

Simon Wedlund, M., M. A. Clilverd, C. J. Rodger, K. Cresswell-Moorcock, N. Cobbett, P. Breen, D. Danskin, E. Spanswick, and J. V. Rodriguez (2014), A statistical approach to determining energetic outer radiation-belt electron precipitation fluxes, *J. Geophys. Res. Space Physics*, *119*, 3961–3978, doi:10.1002/2013JA019715.

Spjeldvik, W. N., and R. M. Thorne (1976), Maintenance of the middle-latitude nocturnal D-layer by energetic electron precipitation, *Pure Appl. Geophys.*, *114*(4), 497–508, doi:10.1007/BF00875646.

Summers, D., B. Ni, and N. P. Meredith (2007), Timescales for radiation belt electron acceleration and loss due to resonant wave-particle interactions: 2. Evaluation for VLF chorus, ELF hiss, and electromagnetic ion cyclotron waves, *J. Geophys. Res.*, *112*, A04207, doi:10.1029/2006JA011993.

Thorne, R. M. (2010), Radiation belt dynamics: The importance of wave-particle interactions, *Geophys. Res. Lett.*, *37*, L22107, doi:10.1029/2010GL044990.

Turunen, E., P. T. Verronen, A. Seppälä, C. J. Rodger, M. A. Clilverd, J. Tamminen, C. F. Enell, and T. Ulich (2009), Impact of different energies of precipitating particles on NO_x generation in the middle and upper atmosphere during geomagnetic storms, *J. Atmos. Sol. Terr. Phys.*, *71*, 1176–1189, doi:10.1016/j.jastp.2008.07.005.

Verronen, P. T., A. Seppälä, E. Kyrölä, J. Tamminen, H. M. Pickett, and E. Turunen (2006), Production of odd hydrogen in the mesosphere during the January 2005 solar proton event, *Geophys. Res. Lett.*, *33*, L24811, doi:10.1029/2006GL028115.

Verronen, P. T., C. J. Rodger, M. A. Clilverd, and S. H. Wang (2011), First evidence of mesospheric hydroxyl response to electron precipitation from the radiation belts, *J. Geophys. Res.*, *116*, D07307, doi:10.1029/2010JD014965.

Weeks, L. H., R. S. Cuikay, and J. R. Corbin (1972), Ozone measurements in the mesosphere during the solar proton event of 2 November 1969, *J. Atmos. Sci.*, *29*, 1138–1142.

Whittaker, I. C., R. J. Gamble, C. J. Rodger, M. A. Clilverd, and J.-A. Sauvaud (2013), Determining the spectra of radiation belt electron losses: Fitting DEMETER electron flux observations for typical and storm times, *J. Geophys. Res. Space Physics*, *118*, 7611–7623, doi:10.1002/2013JA019228.

Whittaker, I. C., M. A. Clilverd, and C. J. Rodger (2014a), Characteristics of precipitating energetic electron fluxes relative to the plasmapause during geomagnetic storms, *J. Geophys. Res. Space Physics*, *119*, 8784–8800, doi:10.1002/2014JA020446.

Whittaker, I. C., C. J. Rodger, M. A. Clilverd, and J.-A. Sauvaud (2014b), The effects and correction of the geometric factor for the POES/MEPED electron flux instrument using a multisatellite comparison, *J. Geophys. Res. Space Physics*, *119*, 6386–6404, doi:10.1002/2014JA020021.

Wissing, J. M., and M.-B. Kallenrode (2009), Atmospheric Ionization Model Osnabrück (AIMOS): A 3-D model to determine atmospheric ionization by energetic charged particles from different populations, *J. Geophys. Res.*, *114*, A06104, doi:10.1029/2008JA013884.

Wüest, M., R. A. Frahm, J. K. Jennings, and J. R. Sharber (2005), Forecasting electron precipitation based on predicted geomagnetic activity, *Adv. Space Res.*, *36*, 2445–2450, doi:10.1016/j.asr.2003.12.014.

Yando, K., R. M. Millan, J. C. Green, and D. S. Evans (2011), A Monte Carlo simulation of the NOAA POES medium energy proton and electron detector instrument, *J. Geophys. Res.*, *116*, A10231, doi:10.1029/2011JA016671.